Three-dimensional velocity map imaging of KBr surface photochemistry

Sven P. K. Koehler,[a] Yuanyuan Ji,[a] Daniel J. Auerbach[b] and Alec M. Wodtke*[a]

Received 14th May 2009, Accepted 3rd June 2009
First published as an Advance Article on the web 17th June 2009
DOI: 10.1039/b909579a

We have combined the velocity map imaging technique with time-of-flight measurements to study the surface photochemistry of KBr single crystals. This approach yields 3-dimensional velocity distributions of Br atoms resulting from 193 nm photodesorption. The velocity distributions indicate that at least two non-thermal mechanisms contribute to the photodesorption dynamics. Our experimental geometry also allows us to measure the Br($^2P_{3/2}$) : Br($^2P_{1/2}$) branching ratio, which is found to be 24 : 1.

Ion imaging and the improved velocity map imaging (VMI) techniques[1] have been successfully applied to many gas-phase photodissociation and crossed-beam experiments over the last 20 years.[2] In the simple case of photodissociation, the ionized photofragments are imaged onto a position-sensitive detector and their velocity distribution with respect to the polarization of the dissociation laser can be derived. Experiments on photodesorption from surfaces have so far not used the elegant VMI technique and instead often relied on time-of-flight (TOF) to gain dynamical information about the process under investigation.[3] Some groups have previously used ion and electron imaging methods to study ion-induced desorption processes[4] and photoelectron emission,[5] but these lack the velocity resolution parallel to the surface inherent to the VMI technique. Other groups have recorded two-dimensional spatial images that contain velocity information for surface scattered ions[6] and photo-desorbed neutral molecules[7] in a way reminiscent of ion imaging. Here we report how TOF measurements can be combined with the VMI technique to yield 3-dimensional velocity distributions.

In order to apply the VMI technique to surface photochemistry, we chose to re-visit the laser-induced desorption of Br atoms from KBr single crystals. Radiation-induced desorption of neutral atoms from alkali-halides has been studied experimentally[8] and theoretically.[9,10] It is well established that one-photon absorption in KBr leads to desorption of Br($^2P_{3/2}$) and Br($^2P_{1/2}$) atoms (referred to hereafter as Br and Br*, respectively) with translational energies depending on the photodesorption wavelength.[11] It is believed that photon energies just below the bulk band-gap induce surface excitons. These surface excited states may relax by emitting hyperthermal halogen atoms; the angular and kinetic energy distribution of these atoms is influenced by the exact origin of the atoms, *i.e.* desorption from terraces results in slightly different kinetic energy release than desorption from edges and kinks. In contrast, absorption at shorter wavelengths beyond the bulk band-gap creates excitons in the bulk that may diffuse, by way of an interstitial Br_2^- intermediate, to the surface, resulting in emission of near-thermal halogen atoms.[11] The Br : Br* branching ratio at 193 nm has been previously reported to be 1000 : 1.[9]

Using our new three-dimensional surface velocity map imaging (TDS-VMI) setup, we measured the velocity distribution of Br and Br* atoms photo-desorbed from KBr single crystals. These were purchased from ESPI Metals and cleaved in air. Freshly cleaved surfaces were imaged by atomic force microscopy (Veeco Dimension 3000) by randomly sampling a number of 1 × 1 μm areas at various positions on the crystal to ensure that the majority of atomic sites (> 1000 : 1) are located on terraces. Samples are then mounted onto a manipulator and the chamber is pumped down to $\sim 3 \times 10^{-10}$ Torr. To clean and anneal the crystal, we heated it to 400 °C over a period of approximately 30 minutes and then slowly cooled it down to room temperature. The pressure rose to about 3×10^{-9} Torr during heating.

A schematic setup of our instrument is shown in Fig. 1. It is composed of a standard set of VMI ion optics consisting of a repeller, extractor and ground plate. A round, centered opening in the repeller plate is just big enough for the round copper sample holder (attached to the manipulator) whose surface is adjusted to be flush with the repeller plate. The

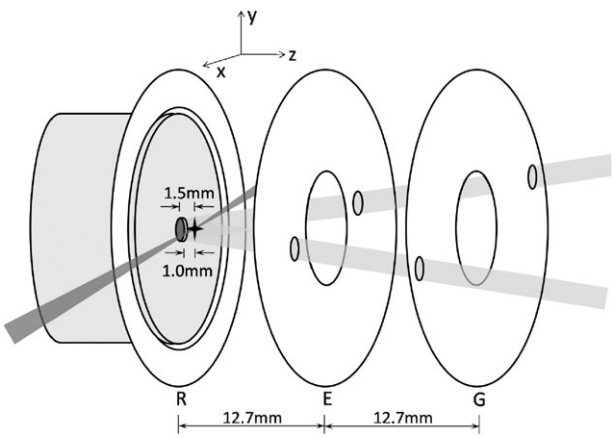

Fig. 1 Schematic of the electrostatic lens assembly of the surface velocity map imaging setup. The dark shaded area in the center of the repeller plate illustrates the recessed KBr surface. The focal point of the resonance enhanced multiphoton ionization (REMPI) laser is 1.0 mm above the repeller plate (R) and 1.5 mm above the KBr surface. The illuminated area is 6 mm in diameter. Small holes in the extractor (E) and ground plate (G) are for desorption laser access only.

[a] *Department of Chemistry and Biochemistry, University of California, Santa Barbara, CA 93106, USA. E-mail: wodtke@chem.ucsb.edu; Fax: +1 (1)805 893 4120; Tel: +1 (1)805 893 8085*
[b] *Gas Reaction Technologies, 861 Ward Dr., Santa Barbara, CA 93111, USA. E-mail: auerbach@grt-inc.com; Fax: +1 (1)408 273 6011; Tel: +1 (1)805 696 6660*

repeller and sample holder are in electrical contact. The sample itself is recessed 0.5 mm behind the front surface of the sample holder/repeller plate and optically accessed by a centered hole 6 mm in diameter.

The optical excitation and detection geometry is of particular importance as it ensures the unbiased and simultaneous detection of the desorption products emerging from the surface in different directions. The output of a 193 nm ArF excimer laser (GAM/EX5), attenuated by means of fine wire mesh to a pulse energy of 30 μJ is incident on the surface at an angle of 45°. All angles are given with respect to the surface normal which is referred to as the *Z*-axis. The laser beam covers the entire exposed KBr crystal, which is roughly 6 mm in diameter. Halogen atoms are ejected and subsequently detected 1.5 mm in front of the crystal. Variation of the time delay between photodesorption and detection laser yields TOF profiles that are used in the following analysis, whereas the ion flight times to the micro-channel plate (MCP) are only used to achieve mass selectivity. Halogen atoms are ionized using 2 + 1 resonance enhanced multiphoton ionization (REMPI) induced by a probe laser pulse at a wavelength of ~235 nm. To produce this light, we combine the frequency-tripled output of a Nd : YAG laser with the output of a second Nd : YAG pumped dye laser operating at 684.22 and 697.56 nm in a β-barium borate (BBO) crystal. We chose the 6p $^4P^\circ_{3/2} \leftarrow \leftarrow {}^2P^\circ_{3/2}$ (Br) and 6p $^2S^\circ_{1/2} \leftarrow \leftarrow {}^2P^\circ_{1/2}$ (Br*) two-photon resonances at 233.6 nm and 235.2 nm, respectively. The 5 mm diameter REMPI laser beam is focused into the chamber with a 36 cm focal length lens. Assuming Gaussian beams for a two-photon transition, the effective ionization region is roughly cylindrical with a length of about 8 mm and a diameter of about 45 μm. Note that the laser power (I) dependence of the 2 + 1 REMPI was measured to follow a power law of $I^{1.7}$ for pulse energies between 0.3 and 4 mJ. Typical pulse energies used for REMPI detection were between 1 and 2 mJ.

The TOF measurements provide the *Z*-component of the velocity, v_Z, of the photo-desorbing Br-atoms, while the velocity maps provide the *X*- and *Y*-components. Despite the short TOF distance of 1.5 mm, the inherent TOF resolution that can be obtained in determining v_Z is still high ($\ell/\Delta\ell \sim 33$). Here, ℓ is the distance from the surface to the laser and $\Delta\ell$ is the size of the focussed laser beam. Furthermore, this geometry, *i.e.* with the laser desorption spot dimensions exceeding the size of the detection volume, has the following important advantage: it allows detection of Br-atoms leaving the surface at angles, θ, as large as 63° with respect to the surface normal. As will be shown below, this is sufficient to simultaneously detect the entire angular distribution of bromine atoms emitted from KBr. Our approach is similar to the counter-intuitive "sheet–dot" optical slicing technique used by Chestakov *et al.* for gas-phase VMI experiments.[12] We also point out that the combination of large desorption spot size and small REMPI ionization volume close to the source enhances the signal in these experiments.

After ionization, the bromine ions are accelerated towards a micro-channel plate (MCP) detector coupled to a phosphor screen (Photonis, Inc.) and charge coupled device (CCD) camera (Sony XC7500). In order to calibrate the VMI velocity space, we periodically performed gas-phase photodissociation experiments on HBr and CH_3Br. For HBr, a molecular beam of HBr seeded in He was produced where the KBr crystal is shown in Fig. 1 and directed down the TOF spectrometer as in standard gas-phase VMI experiments. In order to ensure that the electrostatic fields were not altered in this geometry compared to the KBr photodesorption experiments, we also performed gas-phase VMI experiments with pure methyl bromide admitted into the chamber as background gas at a pressure of 3×10^{-7} Torr with the KBr surface in place. The resulting images of the bromine photofragments obtained after CH_3Br photo-dissociation at 234 nm were blurred due to the thermal motion of the parent CH_3Br molecules in directions parallel to the surface but could nevertheless be used to: (1) find suitable voltages to establish VMI conditions, (2) confirm the HBr calibration of the imaging detector's velocity space and (3) verify that the presence of the KBr single crystal does not distort the electrostatic fields of the VMI spectrometer significantly.

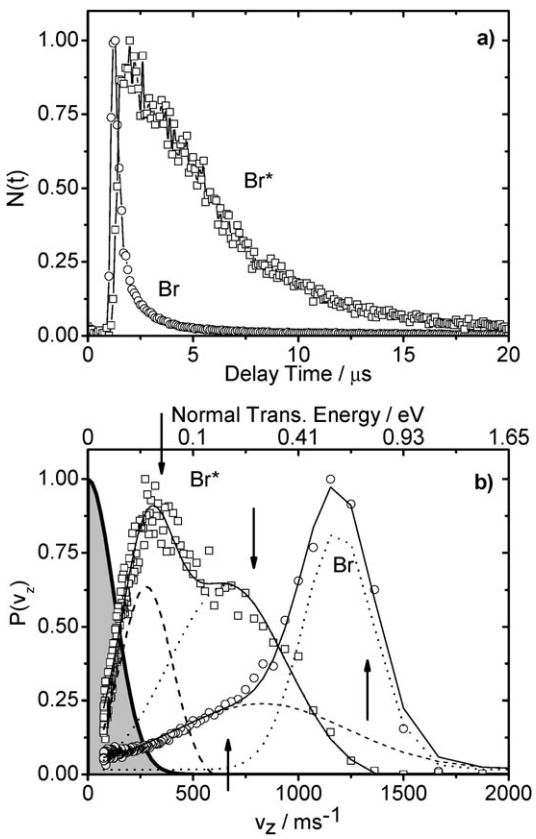

Fig. 2 (a) Br/Br* atom number density *vs.* time-of-flight. KBr surface–REMPI laser distance is 1.5 mm; desorption laser wavelength is 193 nm. (b) Probability distribution in v_Z-space for Br (○) and Br* (□). The dashed and dotted lines result from fitting two Gaussian functions representing "fast" and "slow" channels. Arrows indicate the values of v_Z where velocity map images are shown in Fig. 3, with up-pointing arrows referring to Br and down-pointing arrows referring to Br*. The upper *x*-axis scale shows the corresponding normal translational energy for each value of v_Z. The gray shaded region shows a 1-D thermal speed distribution at 298 K.

Having established suitable velocity map imaging conditions, we recorded TOF spectra for Br and Br* photodesorption products as shown in Fig. 2a. It can be seen that the onset of the Br TOF spectrum is slightly earlier than that for Br*, and that the long-time tail of the Br* signal decays more slowly than that for Br.

After applying the density-to-flux conversion and the appropriate Jacobian,[13] the Z-component of the velocity (v_Z) distributions of Fig. 2b are derived. Inspection of the TOF spectra as well as the derived v_Z distributions reveal two components that contribute to the Br* distribution: one peaking at $\sim$350 m s^{-1} and another at $\sim$800 m s^{-1}. Similarly, the Br distribution also appears to exhibit two components (at $\sim$600 and $\sim$1250 m s^{-1}). We have attempted to make this clearer by fitting the velocity distributions to two Gaussian components. We point out that none of these contributing velocity components can properly be described as thermal, insofar as the thermal velocity distribution of a selected velocity component—in this case v_Z—exhibits a maximum at zero. This can be seen most clearly in Fig. 2b where a 1-D thermal speed distribution is shown for T = 298 K.

The remaining two velocity components, v_X and v_Y, which are parallel to the crystal surface, can be derived from velocity map imaging. Velocity map images are recorded at a number of delay times (*i.e.* at a number of values of v_Z) to yield, in combination, a three-dimensional velocity vector distribution.

Raw velocity map images are recorded in density space due to the means of laser ionization employed here. They are subsequently converted from density to flux distributions, a number of which are shown in Fig. 3 at different delay times (*i.e.* different values of v_Z). The velocity maps all peak at $v_X = v_Y = 0$. Some of the images appear to peak slightly away from the velocity origin, an effect that reflects the error associated with defining this point in velocity space. The velocity origin is determined by comparison to velocity map images of CH_3Br photolysis as described above.

The velocity maps are approximately circular;[14] hence, one may gain insights into the data by averaging these velocity distributions over the azimuth, a quantity we call $c_\parallel$. This leads to a speed distribution for Br or Br* atoms parallel to the surface, which depends parametrically on v_Z: $P(c_\parallel; v_Z)$. These distributions will be reported in detail in a future paper. For now, we present the average speed parallel to the surface, $\langle c_\parallel \rangle$, as a function of v_Z (see Fig. 4a). The 2-D mean thermal speed for Br is given by $(\pi kT/2m)^{1/2}$ and is also shown for reference in Fig. 4a. Here, k is the Boltzmann constant, T is the surface temperature and m is the mass of a Br atom.

In discussing Fig. 2, we pointed out that the data suggests two hyperthermal channels of Br (and Br*) emission. The imaging results shown in Fig. 4a are consistent with this. First of all, only for the very lowest values of v_Z do we observe a near thermal value for $\langle c_\parallel \rangle$. Furthermore, for v_Z values higher than about 400 m s^{-1}, $\langle c_\parallel \rangle$ is higher for the Br channel than for the Br* channel, even at the same value of v_Z. This is a direct reflection of the different parallel forces present in the photo-ejection process for the Br channel in comparison with the Br* channel.

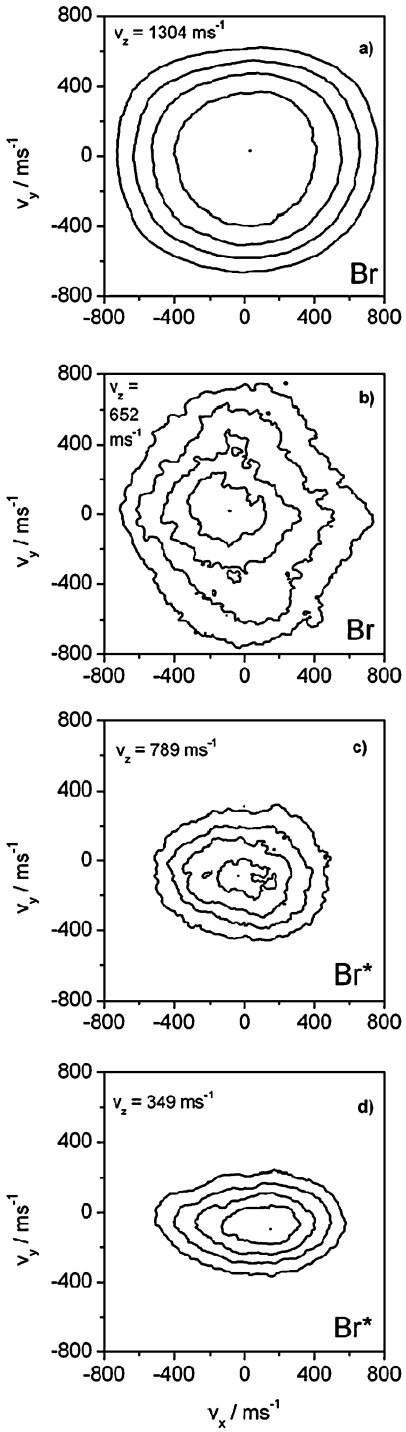

Fig. 3 Selected images at various normal velocities representing the velocity distribution of bromine atoms parallel to the surface. (a) to (b) for Br and (c) to (d) for Br*. Density-to-flux conversion has been applied.

We note that for both spin–orbit channels at low values of v_Z, $\langle c_\parallel \rangle$ rises steeply with v_Z. At high values of v_Z, $\langle c_\parallel \rangle$ rises more gradually. These observations are also suggestive of the existence of two hyperthermal channels of Br and Br* production.

Fig. 4c shows the imaging results represented as angular distributions of the photo-ejected Br or Br* atoms. For

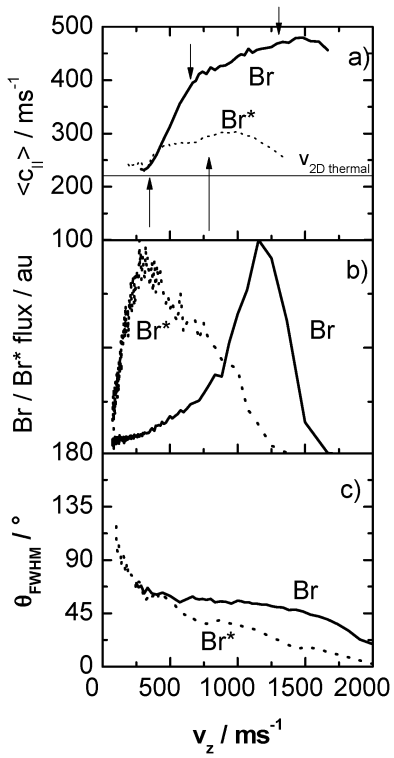

Fig. 4 (a) Averaged mean speed parallel to the surface, $\langle c_{\|} \rangle$, as a function of the normal velocity. Also shown is the mean 2-D speed of thermal bromine atoms. Arrows indicate the values of v_Z where velocity map images are shown in Fig. 3, with up-pointing arrows referring to Br and down-pointing arrows referring to Br*. (b) Surface normal velocity distributions for Br and Br* as in Fig. 2. (c) FWHM angle, θ, of the cone of Br and Br* atoms leaving the surface as a function of v_Z. All graphs: Solid lines correspond to Br data and dotted lines to Br*.

simplicity, we derived the angular FWHM of the azimuthally averaged angular distributions as a function of v_Z. It can be seen that the angular spread of the Br products is roughly independent of v_Z, whereas the Br* angular width decreases rapidly with v_Z. Seeing the v_Z dependence of the angular distributions points out the importance of an experimental geometry that collects products at all recoil angles, if one wishes to derive an accurate branching ratio between the two spin–orbit states of Br. We accomplished this by combining the TDS-VMI results with information on the calibrated signal strengths for Br and Br* detection, obtained by comparing the Br/Br* signals from CH_3Br photodissociation at 234 nm, where the spin–orbit branching ratio has been previously determined: [Br] : [Br*] = 1 ± 0.05.[15] Using this approach, we obtained a branching ratio for 193 nm KBr surface photodesorption of 24 = [Br] : [Br*].

This ratio is more than 40 times smaller than previously reported.[5] We attribute this difference to several possible factors. First, we used a photochemical standard (CH_3Br photolysis) to calibrate our sensitivity to Br and Br*. The authors of ref. 5 apparently used theoretical two-photon line strengths. We also point out that the different geometries used in the two experiments may lead to differences in the apparent branching ratio. The geometry used in this work is designed to detect photodesorption products with equal probability, essentially independent of their recoil angle. In previous work the probe laser was placed further from the surface to enhance TOF resolution. This may have the effect of enhancing sensitivity to desorption channels that emerge with narrow angular distributions peaked about the surface normal. In the case of KBr photodesorption at 193 nm, this tends to suppress detection of the Br* channel in comparison to the Br channel.

Previous experimental and theoretical studies of KBr photolysis suggest that one-photon absorption by KBr single crystals at photon energies less than the bulk band gap creates surface excitons, *i.e.* excited electronic states localized at the KBr vacuum interface. These states are thought to lead to rapid ejection of hyperthermal Br atoms on a time scale much shorter than electron–phonon coupling. This Br-ejection process is thought to leave behind a surface bound electron at the Br vacancy, which may combine with a neighboring K^+ forming a neutral K-atom that is also emitted.† The energy released in Br atom photo-ejection has been theoretically predicted to be ~0.77 eV,[9] consistent with the high translational energy component of the Br kinetic energy distribution seen in this work. The fast Br* channel is shifted to lower translational energies by about the Br spin–orbit splitting,[16] also consistent with a surface exciton photodesorption mechanism.

In this work, we see evidence of two hyperthermal channels for both Br and Br* emission. This shows that the new TDS-VMI results are able to reveal more complex photoejection dynamics in the KBr system than had been previously suspected. There are several possible explanations for the observation of the slower but still hyperthermal channel. Perhaps a fraction of the fast channel suffers secondary collisions with the KBr surface allowing energy transfer from the hot Br atom to the surface. In the limit of low v_Z we do observe near thermal values of $\langle c_{\|} \rangle$, a fact which may be consistent with this explanation. Alternatively, it might be possible that subsurface photoexcitation occurs. Perhaps diffusion of a subsurface exciton, if not too far below the surface, can result in hyperthermal Br ejection due to incomplete energy transfer to the solid. Finally, it may be possible that the diffusion of a bulk exciton to the surface must pass over a reaction barrier to emit a gas-phase Br atom. If the potential energy of this barrier is efficiently channeled into Br translation, hyperthermal emission could result. Definitive answers to these questions await further experimentation and comparison to theory.

In summary, we have demonstrated the usefulness of a three-dimensional velocity map imaging apparatus for the study of surface photo-chemical dynamics. This method reveals two hyperthermal channels in the photodesorption of KBr at 193 nm. The improved geometry of this approach allows us to obtain quantitative branching ratios by accounting for the dependence of the photodesorption angular distribution on desorption velocity. TDS-VMI provides a new tool to the understanding of surface photochemistry.

We acknowledge the support of the US Air Force under grant number FA9550-07-1-0206. SPKK is also grateful to the Alexander von Humboldt Foundation for a Feodor Lynen-Fellowship. YJ thanks the PIRE-ECCI program for a scholarship.

Notes and references

† TDS-VMI results on K-atom photodesorption from KBr at 193 nm will be the subject of a future paper.

1 D. W. Chandler and P. L. Houston, *J. Chem. Phys*., 1987, **87**, 1445; A. T. J. B. Eppink and D. H. Parker, *Rev. Sci. Instrum*., 1997, **68**, 3477.
2 M. N. R. Ashfold, N. H. Nahler, A. J. Orr-Ewing, O. P. J. Vieuxmaire, R. L. Toomes, T. N. Kitsopoulos, I. A. Garcia, D. A. Chestakov, S.-M. Wu and D. H. Parker, *Phys. Chem. Chem. Phys*., 2006, **8**, 26.
3 C. T. Rettner, D. J. Auerbach, J. C. Tully and A. W. Kleyn, *J. Phys. Chem*., 1996, **100**, 13021.
4 P. H. Kobrin, G. A. Schick, J. P. Baxter and N. Winograd, *Rev. Sci. Instrum*., 1986, **57**, 1354.
5 D. Dimitrov, S. Trakhtenberg, R. Naaman, D. J. Smith, P. C. Samartzis and T. N. Kitsopoulos, *Chem. Phys. Lett*., 2000, **322**, 587.
6 D. Corr and D. C. Jacobs, *Rev. Sci. Instrum*., 1992, **63**, 1969.
7 M. Menges, B. Baumeister, K. Al-Shamery, H.-J. Freund, C. Fischer and P. Andresen, *Surf. Sci*., 1994, **316**, 103.
8 W. P. Hess, A. G. Joly, K. M. Beck, D. P. Gerrit, P. V. Sushko and A. L. Shluger, *Appl. Phys. Lett*., 2002, **81**, 1140; M. Szymonski, J. Kolodziej, P. Czuba, P. Piatkowski, A. Poradzisz, N. H. Tolk and J. Fine, *Phys. Rev. Lett*., 1991, **67**, 1906; H. Höche, J. P. Toennies and R. Vollmer, *Phys. Rev. B: Condens. Matter Mater. Phys*., 1994, **50**, 679.
9 W. P. Hess, A. G. Joly, D. P. Gerrit, K. B. Beck, P. V. Sushko and A. L. Shluger, *J. Chem. Phys*., 2001, **115**, 9463.
10 L. F. Chen, Y. Cai and K. S. Song, *Nucl. Instrum. Methods Phys. Res., Sect. B*, 1994, **91**, 614.
11 K. M. Beck, A. G. Joly and W. P. Hess, *Phys. Rev. B: Condens. Matter Mater. Phys*., 2001, **63**, 125423.
12 D. A. Chestakov, S. M. Wu, G. R. Wu, D. H. Parker, A. T. J. B. Eppink and T. N. Kitsopoulos, *J. Phys. Chem. A*, 2004, **108**, 8100.
13 D. J. Auerbach, in *Atomic and Molecular Beam Methods: Volume 1*, ed. G. Scoles, Oxford University Press, Oxford, 1988.
14 The slightly elongated shape in some images may be due to the ionization region not being a perfect spot.
15 T. Gougousi, P. C. Samartzis and T. N. Kitsopoulos, *J. Chem. Phys*., 1998, **108**, 5742.
16 *National Institute of Standards and Technology, NIST Atomic Spectra Database Lines Form*, http://physics.nist.gov/PhysRefData/ASD/lines_form.html.